

Molecular emission around low-mass protostars in the Serpens Main with IRAM 30m

Agnieszka Mirocha^{1,2}, Agata Karska², Lars E. Kristensen³, Marcin Gładkowski^{2,4}, and Michał Żółtowski²

¹ Astronomical Observatory of the Jagiellonian University, ul. Orla 171, 30-244 Kraków, Poland
e-mail: amirocha@doctoral.uj.edu.pl

² Centre for Astronomy, Faculty of Physics, Astronomy and Informatics, Nicolaus Copernicus University, ul. Grudziądzka 5, 87-100 Toruń, Poland

³ Centre for Star and Planet Formation, Niels Bohr Institute and Natural History Museum of Denmark, University of Copenhagen, Øster Voldgade 5-7, DK-1350 Copenhagen K, Denmark

⁴ Nicolaus Copernicus Astronomical Center, ul. Rabiańska 8, 87-100 Toruń, Poland

Received [Month] [Day], 2019; accepted [Month] [Day], 2019

ABSTRACT

Context. The Serpens Main is one of the most studied star forming region containing low-mass protostars. Observations at submillimetre range allow to determine physical and chemical processes around young stellar objects.

Aims. We aim to characterise low-mass protostars' surroundings by analysing the spatial emission of HCN, CN, CS and their isotopologues. This way we can investigate the feedback from protostars and the excitation mechanism of molecules.

Methods. We present 29 arcmin² maps of CN(1-0), HCN(1-0), and CS(3-2) covering the envelope and outflows toward a sample of 13 low-mass protostars using IRAM-30m single dish submillimeter telescope. We obtained spectra of 13 on-source and outflows positions in order to compute HCN(1-0) and CN(1-0) column densities around low-mass protostars. Radiative transfer code RADEX was used to compare observations with the model.

Results. Molecular emission spatial maps show that HCN(1-0) and CS(3-2) are co-spatial with outflow cavity walls. On the other hand, CN emission is stronger at the positions of protostars. As a product of HCN photodissociation CN molecules indicate bow shocks around young stellar objects. The most of protostars in our sample present strong emission in both HCN(1-0) and CN(1-0) lines. Relatively stronger emission in all detected lines is observed around Ser-SMM3, Ser-SMM4 and Ser-SMM6 sources. Weak line of H¹³CN(2-1) was found in two on-source and one outflow position. CN(1-0) and HCN(1-0) column density was estimated as 10¹³ - 10¹⁴ cm⁻².

Key words. astrochemistry – stars: formation – ISM: molecules – ISM: individual objects: Serpens Main – Submillimeter: ISM

1. Introduction

2. Observations

The Serpens Main star forming region was observed with IRAM 30 between 14 and 17 July 2009 (project no. xxx, PI: L. Kristensen). We used the Eight MIXer Receiver (EMIR) as the front-end. The observations were performed in the EMIR bands E090 (molecule HCN 1-0) covering the range 73-117 GHz and E150 (molecules CN 1-0 and CS 3-2) covering the frequencies between 125 and 184 GHz. Due to the EMIR receiver wide bands additional molecular lines of C³⁴S 3-2, H¹³CN 1-0 and H¹³CN 2-1 were also observed. The backend was the Versatile Spectrometer Array (VESPA) autocorrelator and the 1 MHz filterbank reaching the spectral resolution of 39 kHz (E150 band) and 78 kHz (E090 band). The telescope beam size varies from 14'' at 172.68 GHz to 29'' at 86.34 GHz (Table 1). The antenna temperatures were converted to main-beam brightness temperature T_{MB} using the main beam efficiency according to the expression: $T_{\text{MB}} = T_{\text{A}}/\eta_{\text{MB}}$. The exact upper levels energies, line frequencies, beam sizes and beam efficiencies are given in Table 1. Observations included scans of the Ser-SMM1 (centered at $\alpha_{\text{J2000}} = 18^{\text{h}}29^{\text{m}}49.6^{\text{s}}$, $\delta_{\text{J2000}} = +01^{\circ}15'20.5''$ with $V_{\text{LSR}} = +8.5$ km/s) and the Ser-SMM3/Ser-SMM4 (centered at $\alpha_{\text{J2000}} = 18^{\text{h}}29^{\text{m}}56.6^{\text{s}}$,

Table 1. Overview of the observations

Mol.	Trans.	E_{u} (K)	Freq. (GHz)	Beam size ('')	Beam eff. η_{MB}
HCN	1-0	4.25	88.631602	28	0.81
CN	1-0	5.45	113.494921	22	0.78
CS	3-2	14.1	146.969029	16	0.74
C ³⁴ S	3-2	13.9	144.617109	16	0.74
H ¹³ CN	1-0	4.14	86.342274	29	0.81
H ¹³ CN	2-1	12.43	172.677881	14	0.68

Notes. Beam sizes and efficiencies are taken from <http://www.iram.es/IRAMES/mainWiki/Iram30mEfficiencies>

$\delta_{\text{J2000}} = +01^{\circ}14'00.3''$ with $V_{\text{LSR}} = +7.6$ km/s) regions, both 1'×3' OTF maps. The size of the maps is about 300'' × 350'', covering both Ser-SMM1 and Ser-SMM3/Ser-SMM4 regions. The regions are referenced in the article as 'the Northern part' and 'the Southern part' respectively.

Data reduction was carried out with the CLASS package within GILDAS¹. Each spectrum was corrected for the baseline shape, the spike channels were removed and the velocity was re-

¹ See <http://www.iram.fr/IRAMFR/GILDAS>

sampled to a resolution of 0.5 km/s. The baseline fitting of the order of 0 was sufficient for our observations. The rms of extracted spectra values vary from 0.024 K to 0.125 K. Both OTF maps were merged in one map covering 300×350 arcsec. The spectra obtained were exported from the CLASS package and analysed with Python scripts.

3. Results

3.1. Properties of embedded protostars

Ten Class 0/I protostars are present in the observed region. Spectral Energy Distribution (SED) was obtained for each of observed protostars in order to determine its properties.

Most of the protostars in our sample have not been investigated for their properties after *Herschel* observations. Only SMM1, SMM3 and SMM4 were covered by PACS spectroscopy as part of the WISH and DIGIT team surveys (Karska et al. 2013). Based on literature samples the data from the *Herschel* Gould Belt survey (HGBS) project (André et al. 2010) we recalculated SEDs for those sources (Fig. 1).

The linear interpolation was performed while calculating the protostars parameters. The bolometric luminosity was determined by integrating the SEDs over frequency:

$$L_{bol} = \pi d^2 \int F_\nu d\nu \quad (1)$$

where d is the cloud distance of 429 pc (The bolometric temperature was calculated as described in Myers and Ladd 1993:

$$T_{bol} = 1.25 \cdot 10^{-11} \bar{\nu} \quad (2)$$

where $\bar{\nu}$ is the mean frequency given by:

$$\bar{\nu} = \frac{\int \nu F_\nu d\nu}{\int F_\nu d\nu} \quad (3)$$

Table 2 contains the observed protostars parameters as well as the Class classification. The classification was adopted from Enoch et al. 2009 where four types of protostars with envelopes were distinguished. Early Class 0 was defined as a protostar of bolometric temperature lesser than 50K. Protostars characterised by bolometric temperature between 50K and 100K were classified as Late Class 0 protostars. Class I protostars were divided for Early and Late sub-type by the bolometric temperature of 300K.

Most of the observed protostars in the Serpens Main region are very young, embedded sources of Early Class 0. SMM5 and SMM12 were classified as Early Class I YSOs. The SMM6 protostar is the most evolved object in our sample.

3.2. Molecular emission maps

The line maps in the targeted molecules show variety of structures that can be associated with YSOs and a large-scale cloud emission. In the following section we present the large-scale maps of CS $J = 3 - 2$, HCN $J = 1 - 0$ and CN $J = 1 - 0$. Similar maps are shown in the Appendix A.

The integrated line intensity map of HCN $J = 1 - 0$ is shown in Fig. 2. Thirteen low-mass protostars can be distinguished in the field of view. Their positions and properties are shown in Table 2. We have chosen six off-source positions where HCN

² The outflows associated with low-mass protostars were obtained based on CO $J = 6 - 5$ and CO $J = 3 - 2$ observations (Yıldız et al. 2015)

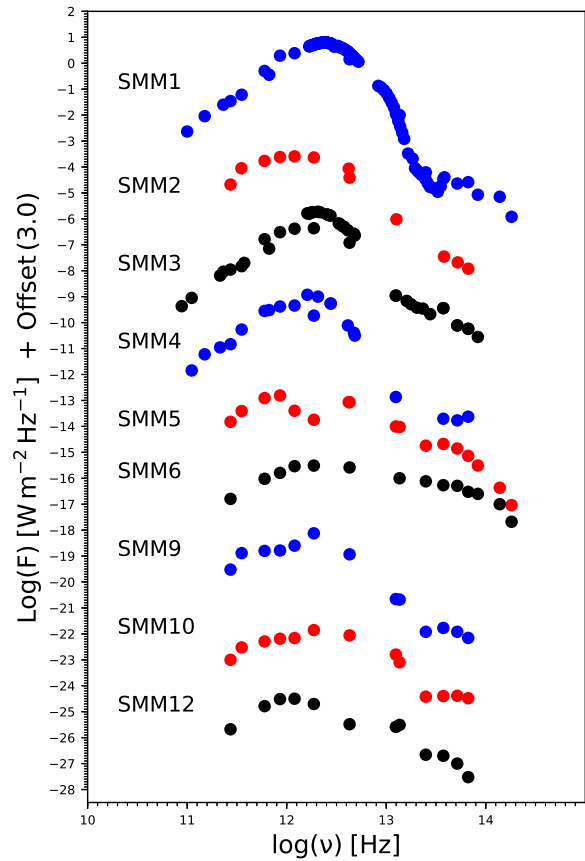


Fig. 1. Serpens Main protostars' spectral energy distribution. There is an offset between plots of $3.0 \text{ W m}^{-2} \text{ s}^{-1}$.

$J = 1 - 0$ or CN $J = 1 - 0$ have the maximum of emission at the location of outflows. Their coordinates and short descriptions is presented in Table 3.

There is no intensively elongated outflow structure from Ser-SMM3 source. The HCN $J = 1 - 0$ map shows extended emission along outflow directions. The HCN $J = 1 - 0$ line was detected at all positions, although it is weak at the positions of Ser-SMM5 and Ser-SMM10. On the other hand, the HCN $J = 1 - 0$ emission is particularly strong around Ser-SMM4 and Ser-SMM9 sources. The emission maxima are detected among the known outflows of Ser-SMM1 and Ser-SMM4 (Yıldız et al. 2015). Especially, at the end of Ser-SMM4 blue outflow (position no. 4) we have significantly strong maximum of the HCN 1-0 radiation.

CS $J = 3 - 2$ line emission map shows similar spatial distribution to HCN $J = 1 - 0$ (Fig. A.3). The most significant elongated structure can be associated with Ser-SMM4 blue-shifted outflow. It is situated at the same place in both maps, extending over $80''$. A similar large-scale structure is detected along Ser-SMM1 outflows, although it is much more distinctive in the HCN $J = 1 - 0$ map. A strong emission around Ser-SMM9 have a circular shape in HCN $J = 1 - 0$ map, however, it has more elongated structure in CS $J = 3 - 2$ line emission which overlaps with the S68N outflows (Kristensen et al. 2010). The peaks of emissions are situated in the different places. HCN $J = 1 - 0$ has relatively strong emission around Ser-SMM4 protostar, but in CS $J = 3 - 2$ line a significant emission towards position no. 3 can be noticed that indicates CN $J = 1 - 0$ local maximum.

CN $J = 1 - 0$ line emission is focused mostly around the positions of protostars (Fig. A.1). The highest local peaks are associated with Class 0 low-mass protostars: Ser-SMM1 (8.2 K km/s),

Table 2. Catalogue of protostars properties

R.A. (J2000.0)	Decl. (J2000.0)	Sbmm source	Other names	T_{bol} (K)	L_{bol} (L_{\odot})	Class
18 29 48.3	+01 16 42.7	SMM9	ISO241, WMW23	46.14	11.69	Early Class 0
18 29 50.0	+01 15 20.3	SMM1	FIRS1, Ser-emb6, Bolo23, EC41	40.35	108.72	Early Class 0
18 29 51.4	+01 16 38.3	SMM5	EC53, WMW24, Ser p3	148.24	4.49	Early Class I
18 29 52.3	+01 15 48.8	SMM10	WMW21	85.09	5.13	Late Class 0
18 29 57.0	+01 13 11.3	SMM4		29.54	13.6	Early Class 0
18 29 57.8	+01 14 05.3	SMM6	EC90, WMW35, SVS20S	526.44	43.39	Late Class I
18 29 59.1	+01 13 14.3	SMM12		100.87	6.68	Early Class I
18 29 59.6	+01 13 59.2	SMM3		42.39	27.49	Early Class 0
18 30 00.5	+01 12 57.8	SMM2	Ser-emb4, Bolo28	41.6	5.1	Early Class 0
18 30 01.9	+01 15 09.2	SMM8			0.068 ^a	

Coordinates taken from Suresh et al. 2016, except S68N (Enoch et al. 2007) and SMM8 (Lee et al. 2014).

References: ^a Dionatos et al. 2010

Table 3. Properties of the selected off-source positions

Pos.	R.A. (J200)	Decl. (J200)	Remarks
1	18:29:45.47	+01:15:53.5	SMM1 blue-shifted outflow in CO(3-2)
2	18:29:54.66	+01:13:19.5	max. CN(1-0), SMM4 blue-shifted outflow in CO(3-2)
3	18:29:50.33	+01:13:68.5	max. HCN(1-0), SMM4 blue-shifted
4	18:29:43	+01:16:41.5	outflow visible in C ³⁴ S(3-2)
5	18:29:56.13	+01:14:14.5	max. CN(1-0), SMM9 surroundings

Ser-SMM3 (15.9 K km/s), Ser-SMM4 (14.1 K km/s) and Ser-SMM6 (15.3 K km/s). The spatial distribution is qualitatively different compared to the HCN $J = 1 - 0$ map. The strongest emission characterises the dense surroundings of Ser-SMM3, Ser-SMM6 and Ser-SMM4 sources while the northern part of this region does not show such a distinct emission in the HCN $J = 1 - 0$ line. On the other hand, dense emissive region of the Ser-SMM9 source is significantly weaker in CN $J = 1 - 0$ line. CN $J = 1 - 0$ map can be characterised by compact, condensed emission without any strongly elongated structures. The H¹³CN $J = 1 - 0$ line exhibits similar morphological distribution as CN(1-0) and C³⁴S(3-2).

In the presence of the UV radiation, HCN molecule photodissociates into CN molecule and H atom (Stäuber et al. 2005). Thus, combined map of these molecules can indicate regions with stronger UV radiation. We present a large-scale map of CN $J = 1 - 0$ to HCN $J = 1 - 0$ flux ratio (Fig. 3). The image of CN emission has been resampled to beam size of HCN in order to compare the same emitting regions. CN/HCN ratio is relatively low around the brightest submillimetre source Ser-SMM1. Similarly, at the dense area of Ser-SMM9 surrounding a significantly weaker CN/HCN emission can be noticed. On the other hand, it peaks at the Northern part of the map around rather faint Ser-SMM5 source. At the Southern part high CN/HCN ratio emission is more extended than in the Northern part. It expands from Ser-SMM3 and Ser-SMM6 area to the North. High CN/HCN ratio can also be found on the edges of the image but it is probably caused by different size of the CN and the HCN maps.

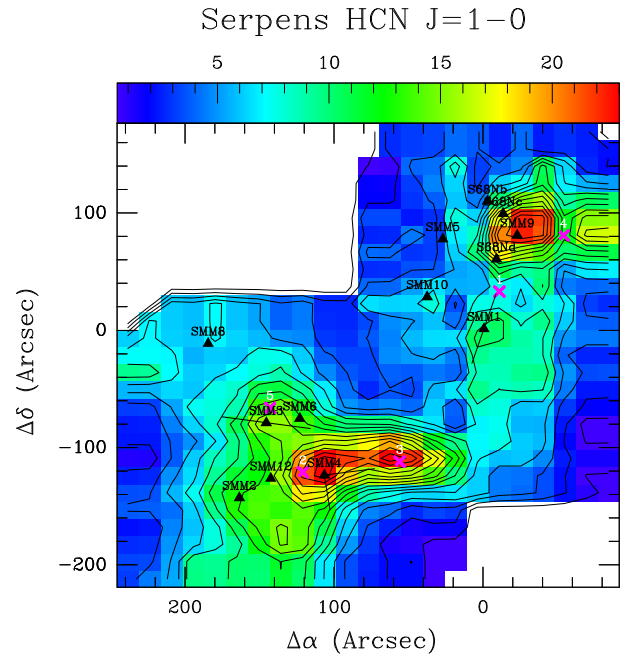


Fig. 2. Emission of the HCN(1-0) in the Serpens Main region. Black triangles show the positions of the protostars (Suresh et al. 2016), whereas the black lines show the associated outflow directions (Yıldız et al. 2015). Outflow positions were displayed as purple crosses.

The low energy level of HCN ($E_u = 4.25$ K) traces cold, high-density gas. HCN has previously been shown to be a good tracer of molecular outflows activity (Walker-Smith et al. 2014). Similar spatial distribution is presented in the CS map. It means that both species trace the gas of the same properties. The CN line is similarly low-energetic, however it peaks in different areas than HCN and CS. CN as a product of HCN photodissociation indicates other properties of low-mass protostars surroundings (Section 4).

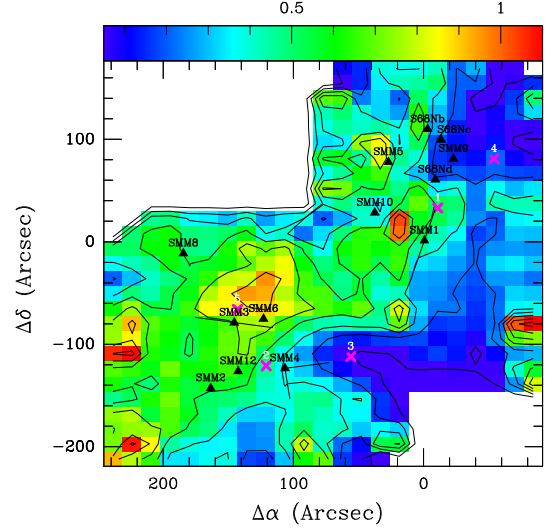
To summarise, spatial distribution of different lines emission varies depending on the observed molecule. The most distinct differences can be noticed between HCN and CN map. Most of the sources show high flux values in both molecules (Table 4). However, they present unequal levels which indicates regions of different properties. In order to better understand this issue we analyse the molecular line profiles in the Section 3.2.

Table 4. Integrated fluxes of the detected protostars

Source	Line	Line freq. ^a (MHz)	Flux ^b (K)	Column dens. (cm ⁻²)
SMM1	CN 1-0	113487.66	6.53	1.3×10^{15}
	HCN 1-0	88629.53	6.78	1.9×10^{14}
	CS 3-2	146964.15	6.93	7.9×10^{13}
	C ³⁴ S 3-2	144612.88	1.39	1.7×10^{13}
	H ¹³ CN 1-0	86337.74	1.28	no data
	H ¹³ CN 2-1	172708.89	0.03	no data
SMM2	CN 1-0	113488.17	10.58	2.2×10^{15}
	HCN 1-0	88629.77	13.98	4.0×10^{14}
	CS 3-2	146965.22	8.03	9.1×10^{13}
	C ³⁴ S 3-2	144613.51	1.15	1.4×10^{13}
	H ¹³ CN 1-0	86337.94	2.46	no data
	H ¹³ CN 2-1	not detected		
SMM3	CN 1-0	113488.19	13.26	2.7×10^{15}
	HCN 1-0	88629.61	12.48	3.6×10^{14}
	CS 3-2	146966.10	10.04	1.1×10^{14}
	C ³⁴ S 3-2	144613.41	0.37	4.4×10^{12}
	H ¹³ CN 1-0	86337.92	0.98	no data
	H ¹³ CN 2-1	not detected		
SMM4	CN 1-0	113488.05	13.06	2.7×10^{15}
	HCN 1-0	88629.61	20.20	5.7×10^{14}
	CS 3-2	146965.44	19.81	2.2×10^{14}
	C ³⁴ S 3-2	144613.74	0.02	1.9×10^{11}
	H ¹³ CN 1-0	86337.80	2.10	no data
	H ¹³ CN 2-1	172673.09	0.26	no data
SMM5	CN 1-0	113488.05	2.57	no data
	HCN 1-0	88629.53	3.71	1.1×10^{14}
	CS 3-2	146965.03	2.33	no data
	C ³⁴ S 3-2	144613.14	0.07	7.9×10^{11}
	H ¹³ CN 1-0	86337.76	0.70	no data
	H ¹³ CN 2-1	not detected		
SMM6	CN 1-0	113487.76	11.48	2.4×10^{15}
	HCN 1-0	88629.61	11.85	3.4×10^{14}
	CS 3-2	146965.03	9.37	1.1×10^{14}
	C ³⁴ S 3-2	144613.25	0.54	6.4×10^{12}
	H ¹³ CN 1-0	86336.53	0.16	no data
	H ¹³ CN 2-1	172673.69	0.02	no data
SMM9	CN 1-0	113487.64	4.82	9.9×10^{14}
	HCN 1-0	88628.98	12.55	no data
	CS 3-2	146963.87	13.75	no data
	C ³⁴ S 3-2	144612.96	1.17	1.4×10^{13}
	H ¹³ CN 1-0	86337.65	1.61	no data
	H ¹³ CN 2-1	172673.14	0.04	no data
SMM10	CN 1-0	113487.58	2.89	5.9×10^{14}
	HCN 1-0	88629.53	4.40	1.3×10^{14}
	CS 3-2	146965.06	4.47	5.1×10^{13}
	C ³⁴ S 3-2	1144613.19	0.35	4.2×10^{12}
	H ¹³ CN 1-0	86337.72	0.98	no data
	H ¹³ CN 2-1	not detected		
SMM12	CN 1-0	113488.17	10.58	2.2×10^{15}
	HCN 1-0	88629.77	13.98	4.0×10^{14}
	CS 3-2	146965.06	10.30	1.2×10^{14}
	C ³⁴ S 3-2	144613.39	0.93	1.1×10^{13}
	H ¹³ CN 1-0	86337.94	2.46	no data
	H ¹³ CN 2-1	not detected		

^a Line frequency at the main peak position.^b Integrated flux above 3σ .

Serpens CN J=1-0 divided by HCN J=1-0

**Fig. 3.** Emission of the divided fluxes CN(1-0)/HCN(1-0) in the Serpens Main region. Black triangles show the positions of the protostars (Suresh et al. 2016), whereas the black lines show the associated outflow directions (Yıldız et al. 2015). Outflow positions were displayed as purple crosses.

3.3. Line profiles

We selected 14 representative on-source and off-source positions for a detailed analysis (Fig. 4). Nine of them are corresponding to the protostars positions, the other five off-source positions were selected based on local maximum of the flux.

The mean region is consistent with HCN 1-0 beam size (27.8") for all molecules. In the majority of our sources five of targeted lines were detected: CN(1-0), HCN(1-0), CS(3-2), C³⁴S(3-2) and H¹³CN(1-0). The line is considered to be detected if there is an emission at the level of at least 3σ . A weak emission from H¹³CN(2-1) was found at the positions of four sources and it is not included in the Figure.

The strongest emission occurs in HCN 1-0, CN 1-0 and CS 3-2 lines and it was detected at the position of all of the sources. The emission in the other lines was multiplied in order to compare profiles between different molecules. In HCN, CN species and their isotopologues a few different velocity components can be identified what indicates the hyperfine splitting. This occurs if a molecule has a non-zero nuclear spin so there is also an interaction between the nuclear spin and the electronic angular momentum. The most distinct splitting can be spotted in the CN $J = 1 - 0$ profiles with five separate components situated between -70 km/s and 18 km/s. The HCN 1-0 line is characterised by three components with low separation situated in the range of -2 km/s – 16 km/s.

Ser-SMM1, Ser-SMM9, and Ser-SMM10 sources have wide spectral lines, while others exhibit narrow line profiles. Spectra extracted from Positions no. 1, 4 and 5 shows prominent blue-shifted wings what can be associated with outflows. Similar structure can be noticed in the Ser-SMM3 (panel no. 7) CS 3-2 and HCN 1-0 profiles.

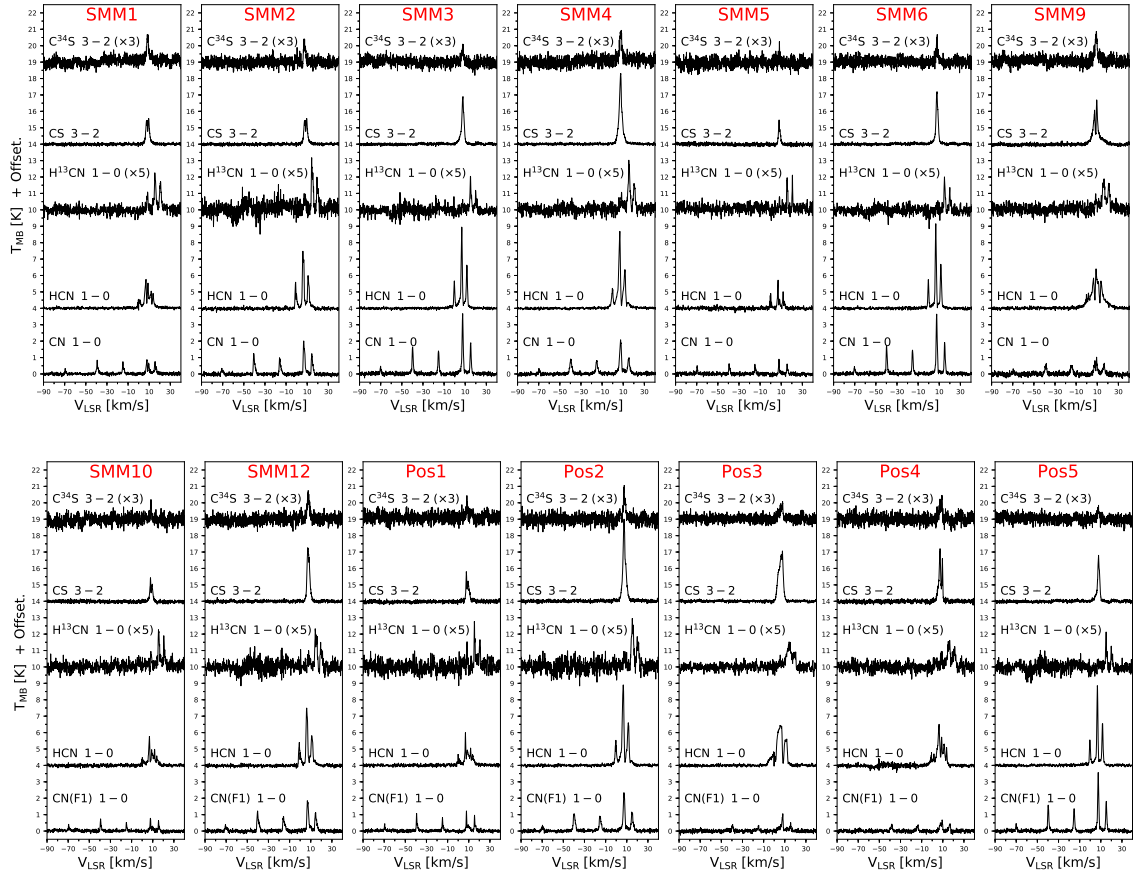


Fig. 4. Serpens Main sources spectra of $C^{34}S(3-2)$, $CS(3-2)$, $H^{13}CN(1-0)$, $HCN(1-0)$ and $CN(1-0)$ lines.

4. Analysis

4.1. Lines column densities

Table 4 shows fluxes integrated from the average line profile at the positions of known protostars. Flux calculation in individual lines allows us to determine the column density of a given transition. The column density of the upper level N_{up} of each observed line was calculated based on following relation:

$$N_u = \beta \frac{\nu W}{A} \quad (4)$$

where $\beta = 1937 \text{ cm}^{-2}$ and $W = \int T_{mb} dV$ is the integrated intensity of the emission line. The frequency ν should be given in GHz.

The column densities of the upper level of $CN J = 1 - 0$ and $HCN J = 1 - 0$ transitions are presented in Table 4. In the closest surroundings of low-mass protostars $CN J = 1 - 0$ is stronger than the lowest transition line of HCN . The column density of $CN J = 1 - 0$ varies between $10^{14} - 10^{15} \text{ cm}^{-2}$, while in the column density of the HCN 's lowest transition reaches 10^{14} cm^{-2} . Except for the Ser-SMM9 and the Ser-SMM10 neighbourhood, $HCN J = 1 - 0$ line column density is an order of magnitude lower than the column density of the equivalent CN transition. This result provides a clue to better understand of the low-mass protostars chemistry.

4.2. RADEX modelling

Molecules column densities can be independently determined using molecular excitation models. Line ratio can provide ad-

ditional information concerning physical properties of the observed gas.

The non-LTE radiative transfer code RADEX (van der Tak et al. 2007) was run in order to prepare sets of molecular excitation models. The CN and HCN molecules column density ratio was the only free parameter. HCN column density was chosen as 10^8 cm^{-2} in order to ensure optically thin emission. CN column density parameter varies from 10^6 cm^{-2} to 10^{10} cm^{-2} what translates into N_{CN}/N_{HCN} in following limits: $10^{-2} - 10^2$. The sets of models were developed assuming a line width of 1.0 km s^{-1} , hydrogen densities of $n_{H_2} = 10^3 \text{ cm}^{-3}$, $n_{H_2} = 10^4 \text{ cm}^{-3}$ and $n_{H_2} = 10^5 \text{ cm}^{-3}$ and kinetic temperatures of $T_{kin} = 30 \text{ K}$, $T_{kin} = 75 \text{ K}$ and $T_{kin} = 200 \text{ K}$. The molecular data files used during modelling were procured from the Leiden Atomic and Molecular Database (LAMDA, Schöier et al. 2005).

Fig. 5 presents one exemplary set of models of CN/HCN column density ratio versus the modelled line intensities ratio for hydrogen densities of $n_{H_2} = 10^5 \text{ cm}^{-3}$ and kinetic temperatures of $T_{kin} = 200 \text{ K}$. The rest of the models are shown in the Appendix B. CN/HCN column density ratio weakly depends on hydrogen density and kinetic temperature in the low limit of those parameters. All presented models show similar properties.

The modelled line intensities are compared with the observations. The observed line intensity ratio covers a range of 0.0-1.0 of the column density ratio in the logarithmic scale. That corresponds to a few times higher CN column density than the same parameter of HCN . This result slightly depends on hydrogen densities and kinetic temperature of the gas (see Table 5).

The sets of models shown in this section indicate that CN/HCN column density ratio covers the range of 1-10 regard-

The model was formulated with two basic assumptions: HCN can only be destroyed through photodissociation and CN reaction with H_2 is the only route to the formation of HCN. In this case the rate of dissociation per unit volume is given by $R_{\text{diss}} = G_0 k_{\text{diss}} n(\text{HCN})$ where photodissociation rate $k_{\text{diss}} = 1.64 \times 10^{-9} s^{-1}$ (Heays et al. 2017). The formation rate of HCN is described by the Equation (2):

$$\frac{dn(\text{CN})}{dt} = G_0 k_{\text{diss}} n(\text{HCN}) - k n(\text{H}_2) n(\text{CN}) \quad (5)$$

where k is the coefficient describing efficiency of CN reaction (Equation 3):

$$k = 4.04 \times 10^{-13} cm^3 s^{-1} \left(\frac{T}{300K}\right)^{2.87} \exp \frac{-820K}{T} \quad (6)$$

Assuming equilibrium and linear relation between a molecule column density and its abundance, UV radiation can be estimated in the units of the interstellar field:

$$G_0 = \frac{k n(\text{H}_2)}{k_{\text{photo}}} \frac{n(\text{CN})}{n(\text{HCN})} \quad (7)$$

All of the results are shown in Table 5. For the upper limit of calculated CN/HCN column density ratio, hydrogen densities of $n_{\text{H}_2} = 10^5 cm^{-3}$ and kinetic temperature of $T_{\text{kin}} = 200 K$, $G_0 = 1.28$ that corresponds to stronger UV field than its average in the interstellar medium.

Acknowledgements. AM, AK and MG are supported by the Polish National Science Center grants 2013/11/N/ST9/00400 and 2016/21/D/ST9/01098.

Fig. 5. RADEX model predictions for the CN/HCN column density ratio for hydrogen densities of $n_{\text{H}_2} = 10^5 cm^{-3}$ and kinetic temperatures of $T_{\text{kin}} = 200 K$ (red line). The observed line intensity ratio is plotted in blue (protostars positions) and green (all positions).

Table 5. The strength of the UV field

$\log_{10}(N[\text{CN}]/N[\text{HCN}])$	$n(\text{H}_2)$ [cm^{-3}]	T_{kin} [K]	G_0
0.03-0.88	10^3	30	$4.80 \times 10^{-16} - 3.39 \times 10^{-15}$
0.06-0.84	10^3	75	$9.45 \times 10^{-8} - 5.69 \times 10^{-7}$
0.00-0.78	10^3	200	$1.28 \times 10^{-3} - 7.68 \times 10^{-3}$
0.16-0.94	10^4	30	$6.47 \times 10^{-15} - 3.90 \times 10^{-14}$
0.08-0.86	10^4	75	$9.89 \times 10^{-7} - 5.96 \times 10^{-6}$
0.04-0.82	10^4	200	$1.40 \times 10^{-2} - 8.42 \times 10^{-2}$
0.20-0.98	10^5	30	$7.09 \times 10^{-14} - 4.27 \times 10^{-13}$
0.18-0.86	10^5	75	$1.25 \times 10^{-5} - 5.96 \times 10^{-5}$
0.22-1.00	10^5	200	$2.12 \times 10^{-1} - 1.28$

References

Suresh, A., Dunham, M. M., Arce, H. G., et al. 2016, AJ, 152, 36

less of excitation conditions. This result suggests that the UV radiation may play an important role around low-mass protostars.

4.3. Astrochemical model

In Section 4.2 we have raised a question about influence of the UV radiation on the surrounding of the observed sources. A simply astrochemical model can be obtained in order to estimate the intensity of the UV field in reference to units of the interstellar UV field G_0 .

As mentioned previously, HCN easily photodissociates into CN molecule and H atom. On the other hand, CN needs more energetic photon for disintegration. In the presence of the UV photons HCN can be dissociated, while CN cannot. This leads to higher abundance of CN molecules and increases CN/HCN column density ratio.

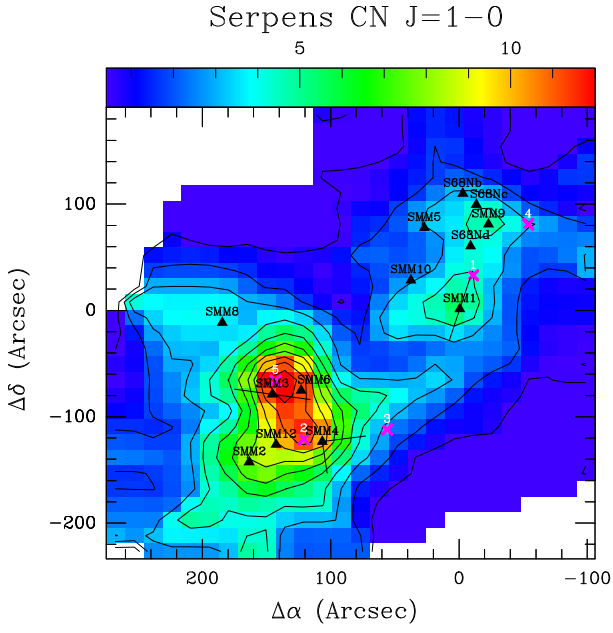


Fig. A.1. Emission of the CN(1-0) in the Serpens Main region. White crosses show the positions of the protostars (Suresh et al. 2016), whereas the white lines show the associated outflow directions (Yıldız et al. 2015). Outflow positions were displayed as purple crosses and the protostars not proceeded in the analysis are marked with yellow crosses (Dionatos et al. 2010).

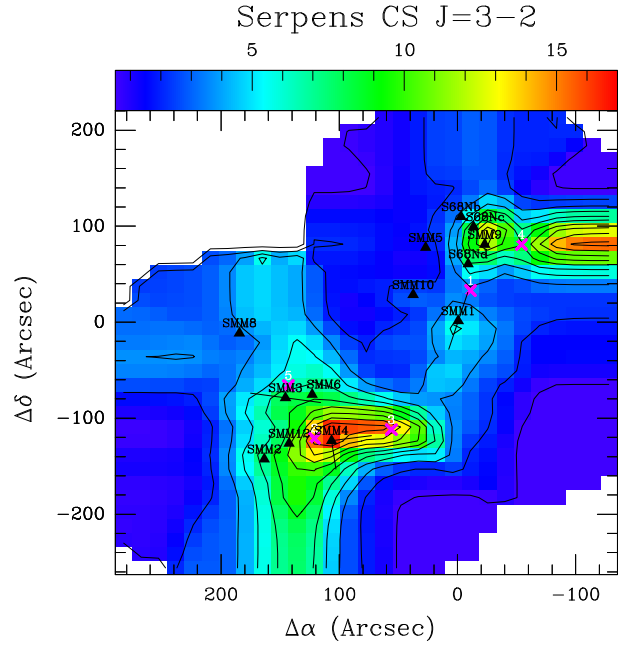


Fig. A.3. Emission of the CS(3-2) in the Serpens Main region. White crosses show the positions of the protostars (Suresh et al. 2016), whereas the white lines show the associated outflow directions (Yıldız et al. 2015). Outflow positions were displayed as purple crosses and the protostars not proceeded in the analysis are marked with yellow crosses (Dionatos et al. 2010).

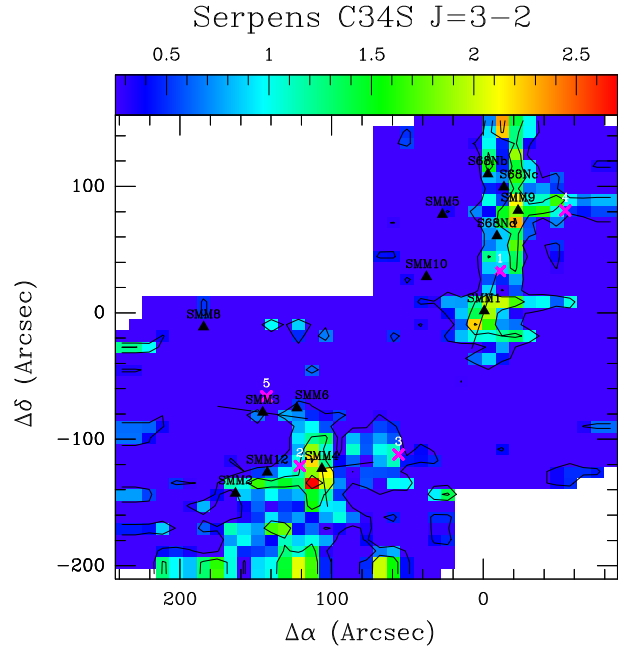


Fig. A.4. Emission of the $C^{34}S(3-2)$ in the Serpens Main region. White crosses show the positions of the protostars (Suresh et al. 2016), whereas the white lines show the associated outflow directions (Yıldız et al. 2015). Outflow positions were displayed as purple crosses and the protostars not proceeded in the analysis are marked with yellow crosses (Dionatos et al. 2010).

Appendix A: Molecular emission maps